

# NH<sub>3</sub> (1, 1) hyperfine intensity anomalies in infall sources

Gang Wu<sup>1,2</sup>, Christian Henkel<sup>2,1</sup>, Dongdong Zhou<sup>1</sup>, Friedrich Wyrowski<sup>2</sup>, Karl M. Menten<sup>2</sup>, and Jarken Esimbek<sup>1</sup>

<sup>1</sup> Xinjiang Astronomical Observatory, CAS 150, Science 1-Street Urumqi, Xinjiang 830011, China  
e-mail: wug@xao.ac.cn

<sup>2</sup> Max-Planck-Institut für Radioastronomie, Auf dem Hügel 69, 53121, Bonn, Germany

Received ...; accepted ...

## ABSTRACT

Identifying infall motions is crucial for our understanding of accretion processes in regions of star formation. The NH<sub>3</sub> (1, 1) hyperfine intensity anomaly (HIA) has been proposed to be a readily usable tracer for such infall motions in star-forming regions harboring young stellar objects at very early evolutionary stages. In this paper, we seek to study the HIA toward fifteen infall candidate regions to assess its reliability as an infall tracer. By using deep observations of the NH<sub>3</sub> (1, 1) transition with the Effelsberg 100 m telescope, HIAs have been identified toward all the targets. Fourteen out of fifteen sources exhibit anomalous intensities either in the inner or outer satellite lines. All the derived HIAs conform to the framework of the existing two models, namely, hyperfine selective trapping (HST) and systematic contraction or expansion motion (CE) models. In our sample of infall candidates, a majority of the HIAs remain consistent with the HST model. Only in three targets, the HIAs are consistent with infall motions under the CE model. Thus HIAs could be used as an infall tracer but seem not highly sensitive to infall motions in our single-dish data. Nevertheless, the emission could be blended with emission from outflow activities. HIAs consistent with the HST model show stronger anomalies with increasing kinetic temperatures ( $T_K$ ), which is expected by the HST model. On the other hand, HIAs consistent with infall motions show little dependence on  $T_K$ . Therefore, HIAs may preferably trace infall of cold gas.

**Key words.** ISM: clouds – ISM: kinematics and dynamics – ISM: molecules – stars: formation

## 1. Introduction

Accretion is a fundamental phenomenon in the process of star formation (e.g. Shu 1977; Mac Low & Klessen 2004). However, observational evidence of gas infall motions has remained inconclusive (e.g. Evans 1999; Evans et al. 2015). Blue-skewed line profiles of optically thick lines serve as readily accessible tracers for infall motions, relying on excitation gradients within the clump (e.g. Leung & Brown 1977; Zhou et al. 1993). Given higher excitation temperatures toward the center, the inward motion of the clump will manifest itself in more pronounced blueshifted emission (Zhou et al. 1993; Evans 1999). Nevertheless, there are also alternative explanations, such as chemical variations and rotation (e.g. Evans 2003). At the same time, blue-skewed line profiles observed by single-dish telescopes may be blended with red-skewed profiles caused by outflow activities. Additionally, the requirement of elevated excitation toward the center implies that the blue-skewed emission as an infall tracer becomes less pronounced for objects in very early evolutionary stages with lower radial changes of the excitation temperature.

Searching for redshifted absorption features against radio or millimeter continuum emission appears to be a promising approach (e.g. Di Francesco et al. 2001; Wyrowski et al. 2012; Yang et al. 2022). The inverse P-Cygni profile, characterized by redshifted absorption and blueshifted emission, is a relatively robust infall indicator, because these profiles largely confirm that the gas moving inwards (redshifted) is in front of the central source. Observations with high angular resolution interferometers are usually required to confirm infall toward the central continuum source (e.g. Beltrán et al. 2022). Because of the optically thick nature of the dust emission at frequencies  $\geq 1$  THz, absorption lines are more readily observed in this frequency range.

Wyrowski et al. (2016) employed the Stratospheric Observatory for Infrared Astronomy (SOFIA) at  $\sim 1.8$  THz and detected redshifted absorption features toward high-mass star formation regions. Additionally, they noted that these redshifted absorption features are often not significantly contaminated by redshifted outflowing gas. However, acquiring new data for these high-frequency absorption lines, which are beyond the capabilities of ground-based telescopes, is not possible after the end of the SOFIA mission.

In all aforementioned methods, optically thin lines are usually required to trace the systemic velocities, delineating the boundary between the blue- and redshifted features and ruling out the possibility of two separate velocity components. Continuous efforts have been made to improve our capacity for detecting infall motions, aiming to achieve a comprehensive understanding of these motions in star-forming regions across a wider range of evolutionary stages and spatial scales. In this study, we test the viability of using ammonia hyperfine intensity anomalies (HIAs) as a promising infall tracer.

The microwave inversion transitions of ammonia (NH<sub>3</sub>) are frequently used tracers in studies of star-forming regions, molecular clouds, and nearby galaxies (e.g., Zhang et al. 1998; Henkel et al. 2005; Lu et al. 2014; Wu et al. 2018). The ground-state para NH<sub>3</sub> ( $J, K$ ) = (1, 1) transition comprises five distinct groups of hyperfine structure (hfs) components, originating from electric quadrupole splitting. These components include the main line ( $\Delta F_1=0$ , where  $F_1$  is the quantum number of the electric quadrupole coupling hyperfines) and four satellite lines ( $\Delta F_1=\pm 1$ ), with two on each side of the main line (Ho & Townes 1983). The presence of weaker magnetic spin-spin interactions results in a total of 18 hyperfine components distributed over the profiles of the five lines (e.g. Rydbeck et al. 1977). Un-

arXiv:2409.12233v1 [astro-ph.GA] 18 Sep 2024

der conditions of local thermodynamic equilibrium (LTE) and optically thin emission, the two inner satellite line groups (ISLs) and outer satellite line groups (OSLs) are anticipated to have the same intensities (26% for each ISL and 22% for each OSL of the main line intensity) (e.g., Ho & Townes 1983). However, the expectation of equal intensities for the ISLs and OSLs is not always valid (e.g. Matsakis et al. 1977; Camarata et al. 2015). Non-LTE populations between the sub-states of the  $\text{NH}_3$  (1, 1) level, which give rise to HIAs, can be attained by (1) hyperfine selective trapping (HST) from  $\text{NH}_3$  (2, 1) to (1, 1) levels (e.g., Matsakis et al. 1977; Stutzki & Winnewisser 1985) and/or (2) systematic contraction or expansion motions (CE) (e.g., Park 2001). It is possible to distinguish between these two models, because they predict different relative intensities of the satellite lines (see Section 4.1). Under the CE model, redshifted/blueshifted photons (due to systematic motions) emitted from one hyperfine transition can be absorbed by another one, resulting in substantial changes in the level populations of the  $\text{NH}_3$  (1, 1) sub-levels. Contraction/expansion can enhance the emission of the two satellite lines on the blue/red side, while suppressing those on the other side (e.g., Park 2001). Thus, the HIA is expected to serve as a tracer of systematic motions without relying on detailed analysis of line shapes (Park 2001).

To summarize, the HIA, as an infall tracer, exhibits two enhanced blueshifted satellite lines, resembling a discrete version of the blue-skewed profile, albeit with different underlying physics. The presence of five well-separated components in the  $\text{NH}_3$  (1, 1) transition enables the straightforward identification of enhanced emission. Furthermore, the HIA is based on the cross-absorption between the hyperfine transitions. In principle, higher excitation toward the center is not required. For example, in the simulations conducted by Park (2001), obvious HIAs were reproduced in an infalling core with a constant temperature of 15 K. This makes the HIA a promising infall tracer of star-forming regions at very early evolutionary stages and also of large scale accretion. In contrast, blue-skewed profiles can reliably trace the infall motion around a hot core (Evans 2003).

Nonetheless, the relative contribution of systematic motions to HIAs remains a matter of debate (e.g. Longmore et al. 2007; Wienen et al. 2018; Zhou et al. 2020). In these studies, HIAs tend to be consistent with the HST model. However, infall motions of the targets in these studies are not confirmed. Hence, in this paper, we seek to investigate HIAs toward fifteen infall candidates, indicated by blue-skewed or redshifted absorption profiles, to test whether the HIA can be used as an infall tracer.

## 2. Targets and observations

### 2.1. Targets

We selected 15 infall candidates from the literature (see Table 1). Blue-skewed profiles were extensively observed in B335, such as by the Institut de Radioastronomie Millimétrique (IRAM) 30 m telescope in  $\text{H}_2\text{CO}$  ( $2_{12}-1_{11}$ ), CS (2–1), (3–2), (5–4) and by the Caltech Submillimeter Observatory (CSO) 10.4 m telescope in  $\text{HCO}^+$  (3–2) with resolutions ranging from 11'' to 28'' (e.g. Zhou et al. 1993). Inverse P-Cygni profiles were also seen in Atacama Large Millimeter/submillimeter Array (ALMA) HCN (4–3) and  $\text{HCO}^+$  (4–3) spectra with a resolution of about 0''.5 (Evans et al. 2015). However, recent high-resolution ALMA observations of optically thin tracers revealed the presence of two velocity components, which could contribute to the double-peaked line profiles (e.g. Cabedo et al. 2021).

Infall indicators were also widely identified in G031.41+0.31. For example, a redshifted absorption profile was identified in the SOFIA  $\text{NH}_3$   $3_{2+}-2_{2-}$  line with a resolution of about 16'' (Wyrowski et al. 2012). Meanwhile, blue-skewed profiles were detected in the  $\text{HCO}^+$  (4–3), HNC (4–3), HCN (4–3) lines observed with the using the Atacama Pathfinder Experiment 12 meter submillimeter telescope (APEX) and the CS (2–1) line observed with the IRAM 30 m telescope with resolutions ranging from 17'' to 27'' (Wyrowski et al. 2016). Inverse P-Cygni profiles were also detected in dense cores with ALMA spectra of  $\text{CH}_3\text{CN}$  ( $12-11$ ) and  $\text{H}_2\text{CO}$  ( $3_{0,3}-2_{0,2}$ ), ( $3_{2,2}-2_{2,1}$ ), and ( $3_{2,1}-2_{2,0}$ ) with resolutions of about 0''.1 (e.g. Beltrán et al. 2022).

The inverse P-Cygni profile in IRAS 18360-0537 was observed near the dust peak MM1 using the Submillimeter Array (SMA) in the CN (2–1) line with a resolution of about 1''.4 (Qiu et al. 2012). Blue-skewed profiles were also identified with the CSO in HCN (3–2) and the Arizona Radio Observatory (ARO) 12 m telescope in  $\text{HCO}^+$  (1–0) with resolutions of 27'' and 70'', respectively (Yoo et al. 2018).

G023.21–0.3, G034.26+0.2, and G035.20–0.7 were selected from Wyrowski et al. (2016). In these three targets, redshifted absorption features were observed using the SOFIA in the  $\text{NH}_3$   $3_{2+}-2_{2-}$  line at a resolution of about 16''. Furthermore, blue-skewed profiles were identified in all three targets through in  $\text{HCO}^+$  (4–3) with APEX with a resolution about 17'' (Wyrowski et al. 2016). As also reported in Wyrowski et al. (2016), in the case of G023.21–0.3, APEX HNC (4–3) observations with a resolution of 16'' revealed blue-skewed profiles. Similarly, in the case of G034.26+0.2, APEX HCN (4–3) observations with a resolution of 17'' showed blue-skewed profiles. As for G035.20–0.7, IRAM 30m  $\text{HCO}^+$  (1–0) observations with a resolution of 28'' revealed the presence of blue-skewed profiles.

BGPS 3604, BGPS 4029, and BGPS 5021 were selected from Calahan et al. (2018). Blue-skewed profiles were observed in the three targets using ARO 12 m single-pointing  $\text{HCO}^+$  (1–0) observations, with a resolution of about 68'' (Calahan et al. 2018). Yang et al. (2021) mapped G029.60–0.63, G053.13+0.09, G081.72+0.57, G082.21–1.53, G121.31+0.64, and G193.01+0.14 with the IRAM 30m telescope at a resolution of about 28''. In all of these six targets, blue-skewed profiles were detected in the  $\text{HCO}^+$  (1–0) line toward the positions showing strongest  $\text{H}^{13}\text{CO}^+$  (1–0) emission (Yang et al. 2021).

### 2.2. $\text{NH}_3$ observations

Deep  $\text{NH}_3$  observations (PI: Gang Wu, project ID: 15-21) were conducted in February 2022 with the Effelsberg 100 m telescope<sup>1</sup>. The K-band double-beam and dual-polarization receiver was employed as the frontend. The facility Fast Fourier Transform Spectrometer (FFTS) was used as backend, which offered two frequency windows with bandwidths of 300 MHz and 65536 channels each. This results in a channel width of about 4.6 kHz, corresponding to a velocity spacing of about  $0.06 \text{ km s}^{-1}$  at 23.7 GHz. The three metastable  $\text{NH}_3$  ( $J, K$ ) = (1, 1), (2, 2), and (3, 3) lines, along with the  $J_{K_a, K_c} = 6_{16}-5_{25}$  water maser transition, were observed simultaneously. Spectral calibration was applied, following the method described by Winkel et al. (2012). NGC 7027 was used to obtain the initial pointing and focus corrections and to calibrate the spectral line flux, assuming a con-

<sup>1</sup> The 100-m telescope at Effelsberg is operated by the Max-Planck-Institut für Radioastronomie (MPIfR) on behalf of the Max-Planck-Gesellschaft (MPG).

tinuum flux density of 5.7 Jy at 23.7 GHz (Ott et al. 1994). At the NH<sub>3</sub> frequencies, the full width at half maximum (FWHM) beam size is about 37'' and the main beam efficiency is 60%. The conversion factor from the flux density scale to the main beam brightness temperature is 1.73 K Jy<sup>-1</sup>. The focus was checked every few hours and pointing was calibrated every hour by observing nearby compact continuum sources. A position-switching mode was used in the observations with the off position at an offset of 900'' of each target in azimuth. Since achieving good signal-to-noise ratios for the NH<sub>3</sub> (1, 1) satellite lines is crucial to establish a robust HIA (e.g. Zhou et al. 2020), the total on + off integration time on each target exceeds 70 minutes and 1- $\sigma$  noise levels are about 50 mK on a  $T_{\text{mb}}$  scale for a channel width of 0.06 km s<sup>-1</sup> (see Table 1). Note that NH<sub>3</sub> (1, 1) hyperfine features were all measured simultaneously, thus ensuring an accurate relative calibration.

The GILDAS/CLASS software developed by IRAM was mainly used for the data reduction. All of the spectra have flat and gently varying baselines so that only linear baselines had to be subtracted.

### 3. Results

Thanks to the long integration times on the targets (see Table 1), all of the NH<sub>3</sub> satellite lines are clearly detected (see Fig. 1). This is important for unambiguously determining the HIAs and distinguishing between the HIA models (see Section 1 and below). As discussed in Zhou et al. (2020), the HIA calculated with peak intensities from Gaussian fittings does not accurately reflect the true anomaly. That is because the red- and blueshifted ISLs (OSLs), which are the combination of Gaussian spectra of three (or two) hyperfine components with different offsets (see the blue vertical lines in Fig. 1), should exhibit different line widths and peak intensities even under LTE and optically thin conditions (see Appendix A in Zhou et al. 2020). We largely follow the recipe described in Zhou et al. (2020) to determine the HIA by the ratio of their red- to blueshifted integrated intensities. Specifically, we first used the combined 18 Gaussian hyperfine components to fit the observed NH<sub>3</sub> (1, 1) spectra. Then, based on the fitted central velocity and velocity dispersion, we defined the integrated velocity ranges (see the red vertical lines in Fig. 1). Finally, we calculated the HIAs of the ISL ( $HIA_{\text{IS}}$ ) and OSL ( $HIA_{\text{OS}}$ ) by the ratio of their redshifted to blueshifted integrated intensities from the observed spectra,

$$HIA_{\text{IS}} = \frac{F_{\text{RISL}}}{F_{\text{BISL}}}, \quad (1)$$

$$HIA_{\text{OS}} = \frac{F_{\text{ROS L}}}{F_{\text{BOS L}}}, \quad (2)$$

where  $F_{\text{RISL}}/F_{\text{ROS L}}$  and  $F_{\text{BISL}}/F_{\text{BOS L}}$  are the integrated intensities of the red- and blueshifted sides of the ISLs/OSLs, respectively. The standard deviation  $\sigma_{\text{HIA}}$  of HIAs is assigned by

$$\sigma_{\text{HIA}} = HIA \times \sigma_{\text{BL}} \times \sqrt{N_{\text{C}}/(F_{\text{R}})^2 + N_{\text{C}}/(F_{\text{B}})^2}, \quad (3)$$

where HIA is either the value of  $HIA_{\text{IS}}$  or  $HIA_{\text{OS}}$ .  $N_{\text{C}}$  is the channel number within the integrated range and  $\sigma_{\text{BL}}$  is the noise level of the baseline.  $F_{\text{R}}$  and  $F_{\text{B}}$  are the integrated intensities of the redshifted and blueshifted sides of the ISLs or OSLs.

The distribution of observed  $HIA_{\text{IS}}$  and  $HIA_{\text{OS}}$  values of the 15 targets is also shown in Fig. 2. Unity indicates no anomaly. In 14 out of 15 targets, either  $HIA_{\text{IS}}$  or  $HIA_{\text{OS}}$  deviate from

unity by more than  $\sigma_{\text{HIA}}$ , and in 10 of these targets, both  $HIA_{\text{IS}}$  and  $HIA_{\text{OS}}$  values exceed  $\sigma_{\text{HIA}}$ . Thus the presence of HIAs is prevalent in our sample. The two dashed lines in Fig. 2 divide the the  $HIA_{\text{IS}}$  and  $HIA_{\text{OS}}$  data into four quadrants: quadrants I ( $HIA_{\text{IS}} > 1$  and  $HIA_{\text{OS}} > 1$ ), II ( $HIA_{\text{IS}} < 1$  and  $HIA_{\text{OS}} > 1$ ), III ( $HIA_{\text{IS}} < 1$  and  $HIA_{\text{OS}} < 1$ ), and IV ( $HIA_{\text{IS}} > 1$  and  $HIA_{\text{OS}} < 1$ ). These quadrants can be utilized to distinguish different HIA models (see Section 4.1). From Fig. 2 we can see that 1 (6.7%), 11 (73.3%), 3 (20%), and 0 data points are located in quadrants I, II, III, and IV (0, 7 (46.7%), 3 (20%), and 0, respectively, considering 1- $\sigma$  uncertainties). These fractions in the four quadrants, based on our deep observations, are generally consistent with previous statistical results (e.g. Wienen et al. 2018; Zhou et al. 2020).

In the cases of IRAS 18360-0537, G031.41+0.31, G034.26+0.2, and G081.72+0.57, there is significant blending between their main lines and ISLs. This may impact the determination of the  $HIA_{\text{IS}}$  if the main line has asymmetric profiles, which contributes differently to the two ISLs. Hereby, we qualitatively discuss the potential corrections for the line blending. Taking IRAS 18360-0537 as an example, as seen in the first panel of Fig. 1 that the asymmetric main line contributes more flux to the blueshifted ISL than to the redshifted ISL. Thus the real  $HIA_{\text{IS}}$  might be larger than the calculated one, as indicated by the arrow in Fig. 2. However, we should note that the length of the arrow is not quantitatively proportional to the corrections, as it is difficult to precisely determine the contribution of the blending main line. For all of these four targets, we labeled the potential corrections with arrows in Fig. 2. We can see that, for G031.41+0.31 and G081.72+0.57, their actual  $HIA_{\text{IS}}$  should be smaller than the calculated one. Thus these corrections do not alter their quadrants. For the other two targets, especially IRAS 18360-0537 whose  $HIA_{\text{IS}}$  is closer to unity, the line blending effect might change their quadrant from II to I.

We should note that changes in the relative intensities of the ISL or OSL may occur due to large opacities. Theoretically, each ISL (OSL) contains three (two) identical hyperfine components, indicated by the blue vertical lines in Fig. 1. However, as previously mentioned, while the intensities of the hyperfine components are the same, the frequency separations between them vary, as represented by the spacing of the blue vertical lines in Fig. 1. In high-opacity scenarios, satellites with closer separations between hyperfine components may achieve saturation more rapidly compared to those with larger separations. Therefore, we also derived the opacities of the ISL and OSL for all the spectra by summing up the opacities of their respective hyperfine components (see Table 1). The ISLs and OSLs in our spectra tend to be optically thin, with the exceptions of those of G035.2-0.7 and G023.21-0.3, which show moderate opacities of about 0.6. Therefore, the opacities should not result in a significant intensity difference between the two ISLs/OSLs.

As discussed in Zhou et al. (2020), the deviations of the HIA defined by peak intensities from the true HIA is getting more pronounced for spectra with narrow linewidths. We can see from Fig. 3, take B335 as an example, that the peak intensity of the blueshifted OSL is larger than that of the redshifted one, just because the separation of the two hyperfine components within the blueshifted OSL is smaller than that of the redshifted OSL (see the blue vertical lines in Fig. 2). From Fig. 2 we see that  $HIA_{\text{OS}}$  of B335 is actually larger than unity (the integrated intensity of the blueshifted OSL is smaller than that of the redshifted one). We refer to the Appendix A in Zhou et al. (2020) for the detailed comparisons between the HIAs defined by peak and integrated

**Table 1.** Targets and observational parameters.

No. (1)	Target (2)	R.A. (J2000) (3)	DEC (J2000) (4)	D(kpc) (5)	on-of (min) (6)	$\sigma_{\text{BL}}$ (K) <sup>†</sup> (7)	$T_{\text{K}}$ (8)	$\tau_{\text{ISL}}$ <sup>††</sup> (9)	$\tau_{\text{OSL}}$ <sup>††</sup> (10)
1	G121.31+0.64	00:36:47.80	63:28:57.0	0.89 <sup>1</sup>	78.0	0.052	22.8±0.1	0.15	0.12
2	G193.01+0.14	06:14:22.90	17:43:26.0	1.91 <sup>1</sup>	195.3	0.034	19.9±0.3	0.08	0.06
3	BGPS3604	18:30:43.92	-09:34:42.2	11.01 <sup>2,3</sup>	114.8	0.050	12.3±0.4	0.26	0.21
4	G023.21−0.3	18:34:54.91	-08:49:19.2	4.60 <sup>4,5</sup>	192.8	0.037	24.0±0.2	0.57	0.45
5	BGPS4029	18:35:54.40	-07:59:44.6	3.54 <sup>2,3</sup>	78.4	0.048	14.1±0.2	0.29	0.23
6	IRAS 18360−0537	18:38:40.74	-05:35:04.0	6.30 <sup>6,7</sup>	78.4	0.054	28.0±0.2	0.33	0.26
7	BGPS5021	18:44:37.07	-02:55:04.4	5.18 <sup>2,3</sup>	78.1	0.048	14.7±0.2	0.41	0.32
8	G029.60−0.63	18:47:32.10	-03:14:10.0	4.31 <sup>1</sup>	78.4	0.056	16.7±0.2	0.23	0.18
9	G031.41+0.31	18:47:34.30	-01:12:46.0	3.75 <sup>8</sup>	77.8	0.065	40.2±0.8	0.20	0.15
10	G034.26+0.2	18:53:18.49	01:14:58.7	1.60 <sup>4,5</sup>	76.3	0.058	46.7±0.6	0.19	0.15
11	G035.20−0.7	18:58:12.93	01:40:40.6	2.20 <sup>4,5</sup>	96.4	0.078	27.3±0.2	0.60	0.47
12	G053.13+0.09	19:29:17.20	17:56:18.0	1.67 <sup>1</sup>	125.7	0.042	21.3±0.2	0.08	0.06
13	B335	19:37:00.43	07:34:06.8	0.16 <sup>9</sup>	95.7	0.060	12.8±0.2	0.41	0.32
14	G081.72+0.57	20:39:01.00	42:22:56.0	1.50 <sup>1</sup>	77.8	0.053	33.2±0.2	0.13	0.10
15	G082.21−1.53	20:49:33.00	41:27:34.0	1.13 <sup>1</sup>	97.0	0.047	11.2±0.3	0.42	0.33

**Notes.** (†) The 1- $\sigma$  baseline noise level on a  $T_{\text{mb}}$  scale for a channel width of about 0.06 km s<sup>-1</sup>. (††) The peak opacities of the inner ( $\tau_{\text{ISL}}$ ) and outer ( $\tau_{\text{OSL}}$ ) satellites. (1) Yang et al. (2021) (2) Svoboda et al. (2016) (3) Calahan et al. (2018) (4) Wyrowski et al. (2016) (5) König et al. (2017) (6) Xu et al. (2021) (7) Wu et al. (2023) (8) Immer et al. (2019) (9) Watson (2020) .

intensity ratios. In addition, at the resolution of 37'', our observations may encompass a number of cloud or velocity components, which are more evident in the case of G31.41+0.31 and IRAS 18360−0537, which show slight deviations from Gaussian profiles (see Fig. 1). While the limited angular resolution of our data is ideal for the determination of the gross HIA, it does not permit an evaluation of the spatial fine structure, eventually revealing more than one velocity component within the targeted area.

## 4. Discussion

### 4.1. Are HIAs sensitive to infall motions?

The HST and CE models predict distinct HIAs (e.g. Zhou et al. 2020). According to the HST model, the intensity of the blueshifted ISL is expected to be stronger than that of the redshifted one, while the redshifted OSL should exhibit stronger intensity than the blueshifted one. Thus  $HIA_{\text{IS}} < 1$  and  $HIA_{\text{OS}} > 1$  (quadrant II; e.g. Stutzki & Winnewisser 1985; Camarata et al. 2015). In the context of the CE model (e.g. Park 2001), for infall motions, both the blueshifted ISL and OSL are anticipated to be stronger than the redshifted two lines, that is  $HIA_{\text{IS}} < 1$  and  $HIA_{\text{OS}} < 1$  (quadrant III). Conversely, for expansion motions, the redshifted ISL and OSL are expected to exhibit stronger intensity simultaneously, that is  $HIA_{\text{IS}} > 1$  and  $HIA_{\text{OS}} > 1$  (quadrant I). As discussed in Zhou et al. (2020), we can employ the HIA quadrant plot of  $HIA_{\text{IS}}$  and  $HIA_{\text{OS}}$  to identify the HIA models (see the different models labeled in the four subregions of Fig. 2).

From Fig. 2, it is noteworthy that all the derived HIAs remain within the framework of the two models, with no data points in the forbidden quadrant IV. However, it is somewhat unexpected that a majority of the HIAs are located in the second quadrant, aligning with the HST model. This indicates that, in our observations, the HST model is the predominant model, even in sources likely harboring infall motions. However, alternative explanations exist. Similar to the case of blue-skewed profiles, they

might be blended with emission from outflows (e.g. Evans 2003; Wyrowski et al. 2016). This phenomenon is also applicable to HIAs, since ammonia emission is also commonly seen in outflows (e.g. Zhang et al. 2007). This could only be further clarified through interferometer observations, which are capable of resolving distinct structures.

There are three data points located in quadrant III, indicating the potential existence of infall motions. For these three sources, infall motions should be widespread within the beam size of about 37''. Increased kinetic temperatures would enhance the HST HIAs (e.g. Stutzki & Winnewisser 1985) and could also lead to more ammonia molecules being excited to the NH<sub>3</sub> (2, 1) level. Consequently, the likelihood of sources to be fit the HST model dominating is heightened. So, HIAs may preferably serve as infall tracers in star-forming regions at early evolutionary stages. However, we do not find a preferred evolutionary stage among these three targets in quadrant III. BGPS 4029, G029.60−0.63, and G031.41+0.31 were reported to be associated with an infrared dark cloud (IRDC) (Peretto & Fuller 2009), Class 0/I YSOs (Yang et al. 2020), and a massive protocluster, respectively (Beltrán et al. 2022). Nevertheless, HIAs may indeed be used as an infall tracer for early evolutionary stages, such as IRDCs.

As mentioned earlier, in the HST model, the ISL and OSL exhibit reversed anomalous intensities ( $HIA_{\text{IS}} < 1$  and  $HIA_{\text{OS}} > 1$ ). In the CE model, both the blueshifted/redshifted ISL and OSL should be weaker/stronger simultaneously for infall/expansion motions ( $HIA_{\text{IS}} < 1$  and  $HIA_{\text{OS}} < 1$  for infall motions,  $HIA_{\text{IS}} > 1$  and  $HIA_{\text{OS}} > 1$  for expansion motions). As a result, using the ratio between the sum of the intensities of the two redshifted satellite lines and the sum of the intensities of the two blueshifted satellite lines, the influence of the HST model (the ISL and OSL exhibit reversed anomalies) would be mitigated and that of the CE model would be enhanced. Therefore we also study the ratio  $HIA_{\text{ISOS}}$ ,

$$HIA_{\text{ISOS}} = \frac{F_{\text{RISL}} + F_{\text{ROS L}}}{F_{\text{BISL}} + F_{\text{BOS L}}}. \quad (4)$$

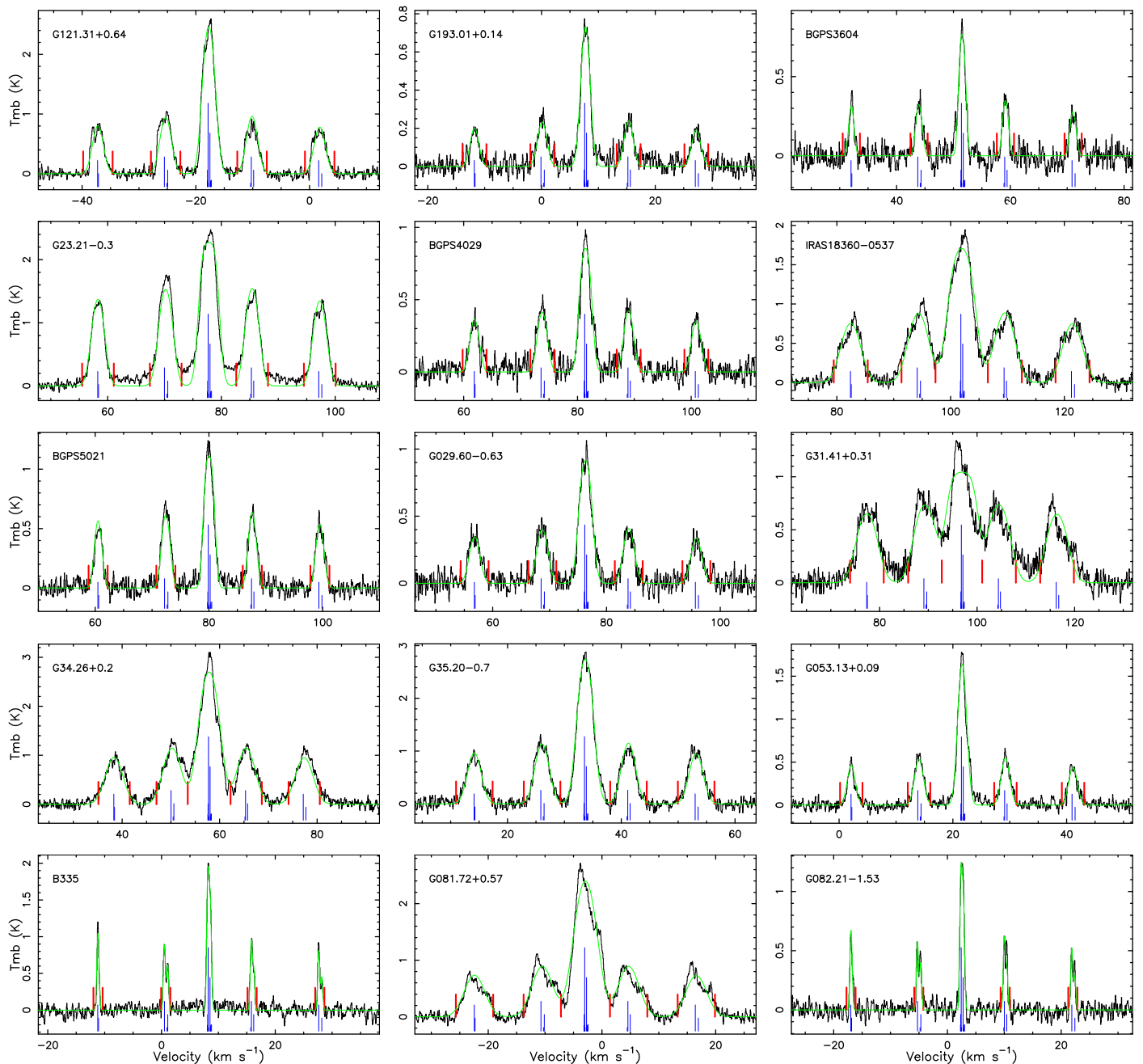


**Fig. 1.** Observed  $\text{NH}_3$  ( $J, K$ ) = (1, 1) spectra. In each panel, the green curve represents the 18-hyperfines fitting result and the blue vertical lines under the spectrum indicate the position of the 18 hyperfine lines and their relative strengths in the optically thin case under conditions of LTE. The red lines denote the integrated ranges used to calculate the HIA. The source name is labeled in the top-left corner of each panel.

We should note that it is not known whether the anomalous fluxes of the blueshifted ISL and the redshifted OSL are precisely equal in the HST model (e.g. Stutzki & Winnewisser 1985).

Fig. 3 shows the distribution of  $HIA_{\text{ISOS}}$ . Eight sources (six, considering uncertainties) out of 15 are consistent with infall motions. Indeed, more sources exhibit consistency with infall motions than those in quadrant III of Fig. 2. This outcome demonstrates that  $HIA_{\text{ISOS}}$  could be a better infall tracer than  $HIA_{\text{IS}}$  and  $HIA_{\text{OS}}$ . However,  $HIA_{\text{ISOS}}$  may also not be a very ideal indicator of infall for our data. Taking uncertainties into account, there are only six reliable data points of  $HIA_{\text{ISOS}}$  consistent with infall motions in this sample of infall candidates. Naturally, the three sources already previously suggested to rep-

resent infall (quadrant III sources in Fig. 2) are part of this subsample.

To summarize, in our single-dish observations, most of the detected HIAs are consistent with the HST model. HIAs could be used as an infall tracer but seem not highly sensitive to infall motions. High-resolution observations would be essential for a more precise assessment of the contaminating impact by outflows.

#### 4.2. HIAs versus kinetic temperature

As we mentioned before, higher temperatures would potentially lead to the dominance of the HST model. In this section, we explore the correlation between HIAs and the kinetic temperature

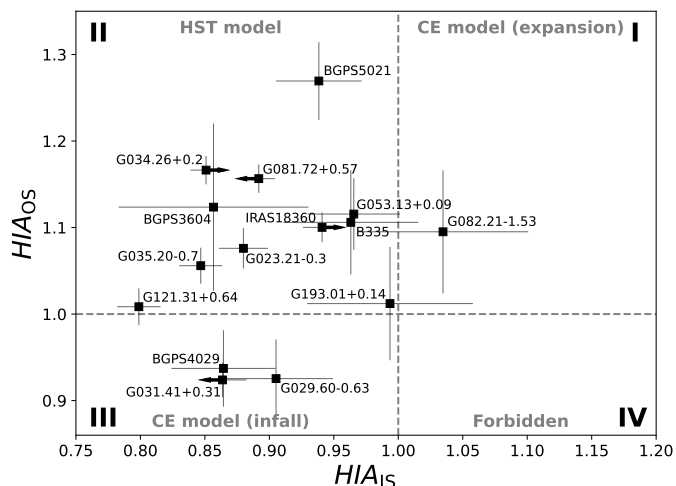


**Fig. 2.** Distribution of the hyperfine intensity anomalies of the inner ( $HIA_{IS}$ ) and outer ( $HIA_{OS}$ ) satellite lines. Arrows indicate potential corrections for the blending of the primary and inner satellite lines. The source name is marked in close proximity to each data point. Gray dashed vertical and horizontal lines divide the panel into four subregions: I for  $HIA_{IS} > 1$  and  $HIA_{OS} > 1$ , II for  $HIA_{IS} < 1$  and  $HIA_{OS} > 1$ , III for  $HIA_{IS} < 1$  and  $HIA_{OS} < 1$ , and IV for  $HIA_{IS} > 1$  and  $HIA_{OS} < 1$ . The models that cause HIAs to be located in these subregions are also labeled.

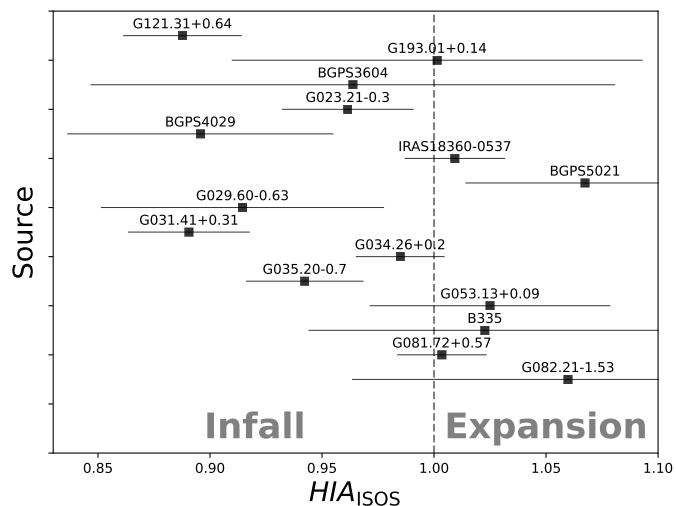


**Fig. 3.** Distribution of the combined hyperfine intensity anomalies. The source name is labeled above each data point.

( $T_K$ ).  $\text{NH}_3$  inversion transitions are an invaluable spectroscopic probe of  $T_K$  (Ho & Townes 1983). We derive the rotational temperature  $T_R$  from the observed para- $\text{NH}_3$  (1, 1) and (2, 2) spectral lines (see Fig. A.1) using the PySpecKit package (Ginsburg & Mirocha 2011), which is a forward-modeling tool for spectral lines. Then,  $T_K$  is calculated following Tafalla et al. (2004) as

$$T_K = \frac{T_R}{1 - \frac{T_R}{42} \ln[1 + 1.1 \exp(-16/T_R)]}. \quad (5)$$

Tafalla et al. (2004) conducted various Monte Carlo simulations involving data of the  $\text{NH}_3$  (1, 1), (2, 1), and (2, 2) transitions to derive an analytical expression to estimate  $T_K$  from  $T_R$ .  $T_K$  can be very well approximated by this equation in the range  $T_K = 5\text{--}20$  K. It is important to note that the applicability of this approximation diminishes at higher temperatures. Fig. 4 shows the

**Table 2.** Parameters for the linear regressions.

Models	Slope ( $\times 10^{-3}$ )	Intercept	$r^\dagger$
(1)	(2)	(3)	
$HIA_{IS}$			
CE	$-0.7 \pm 1.0$	$0.90 \pm 0.04$	-0.43
HST	$-2.0 \pm 1.4$	$0.93 \pm 0.05$	-0.29
$HIA_{OS}$			
CE	$-0.3 \pm 0.3$	$0.94 \pm 0.01$	-0.66
HST	$2.4 \pm 2.3$	$1.08 \pm 0.08$	-0.12
$HIA_{ISOS}$			
CE	$-0.5 \pm 0.5$	$0.92 \pm 0.02$	-0.60
HST	$-0.2 \pm 1.4$	$0.99 \pm 0.05$	-0.17

**Notes.** The regressions were conducted by the SciPy package.

( $\dagger$ ) The correlation coefficient assumes values within a range from -1 (indicating a perfect negative correlation) to +1 (indicating a perfect positive correlation). A correlation coefficient of zero denotes no relationship between the two variables under consideration.

correlations between HIAs ( $HIA_{IS}$ ,  $HIA_{OS}$ , and  $HIA_{ISOS}$ ) and  $T_K$ . The HIAs consistent with the HST model and CE model (infall motions) are emphasized in blue and red colors, respectively. Meanwhile, their linear regression results are also shown in each panel (blue and red lines) and in Table 2.

We first see from the blue data points in panels (a) and (b) of Fig. 4 that  $HIA_{IS}$  and  $HIA_{OS}$  all tend to show rising deviations from unity (indicating higher anomalies) with increasing  $T_K$ , which is expected by the HST model. We should note that the correlations are weak, with correlation coefficients of  $-0.29$  and  $-0.12$  for  $HIA_{IS}$  and  $HIA_{OS}$ , respectively (see Table 2). This may be attributed to the considerable dispersion among these data points, especially  $HIA_{OS}$  determined by the relatively weak OSLs. While the HST model predominantly influences the blue data points, the CE model may also play a minor role, introducing additional uncertainties. For example, the two HIA models produce contrasting predictions concerning the enhancement of the OSLs.

HIAs consistent with infall motions are not expected to exhibit a dependence on  $T_K$ . In our observations, both  $HIA_{IS}$  and  $HIA_{OS}$ , indicated by red color, appear to show a constant value not depending on  $T_K$ . It is essential to note that the sample size is limited, consisting of only three data points. Therefore, subsequent comparisons of potential trends in HIAs against  $T_K$  are tentative. The slope of  $HIA_{IS}$  appears more negative compared to that of  $HIA_{OS}$ . In general, HIAs induced by infall motions (red data points) demonstrate relatively lower sensitivity to  $T_K$  compared to HIAs consistent with the HST model (blue data points in Fig. 4). This outcome implies that HIAs might serve as more effective infall tracers for relatively cold gas, which may help us to understand the large-scale accretion and infall motions in early evolutionary star-forming cores.

Finally, in panel (c) of Fig. 4, we can see from the blue data points, in general, the  $HIA_{ISOS}$  of the targets associated with the HST model, are very close to unity. So,  $HIA_{ISOS}$  could largely weaken the impact of the HST model as explained before (see Fig. 3). This indicates that the anomalous flux to the blueshifted ISL is comparable to that of the redshifted OSL in the HST model. The red data points (i.e. those associated with infall motions) are not affected by such a consideration, since their blueshifted ISLs and OSLs are enhanced simultaneously.



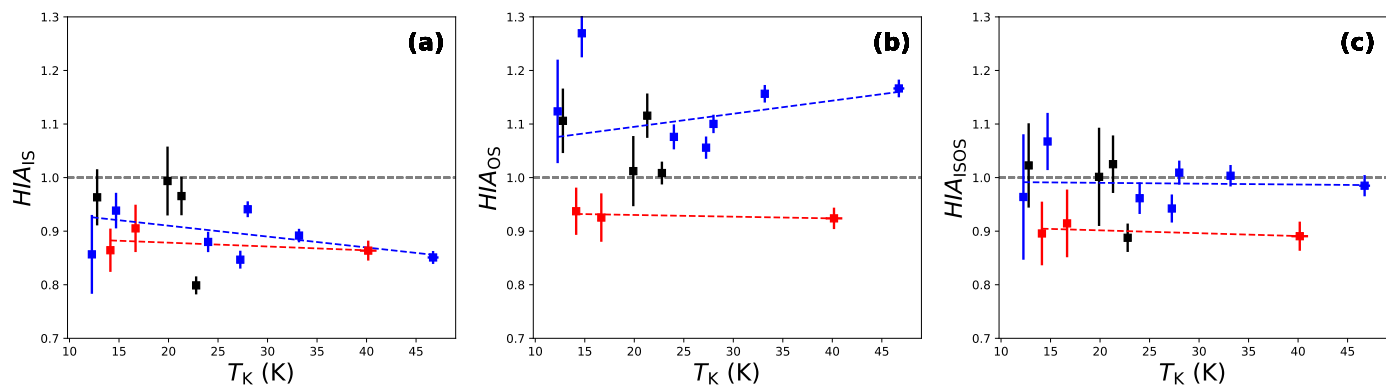


**Fig. 4.** Correlations of  $HIA_{IS}$  and  $T_K$  (panel a),  $HIA_{OS}$  and  $T_K$  (panel b), and  $HIA_{ISOS}$  and  $T_K$  (panel c). The HIAs consistent with the HST model and CE model (infall motions) are emphasized in blue and red colors, respectively. Blue and red lines indicate their linear regression results. Linear fit parameters for the blue and red lines are given in Table 2.

## 5. Summary

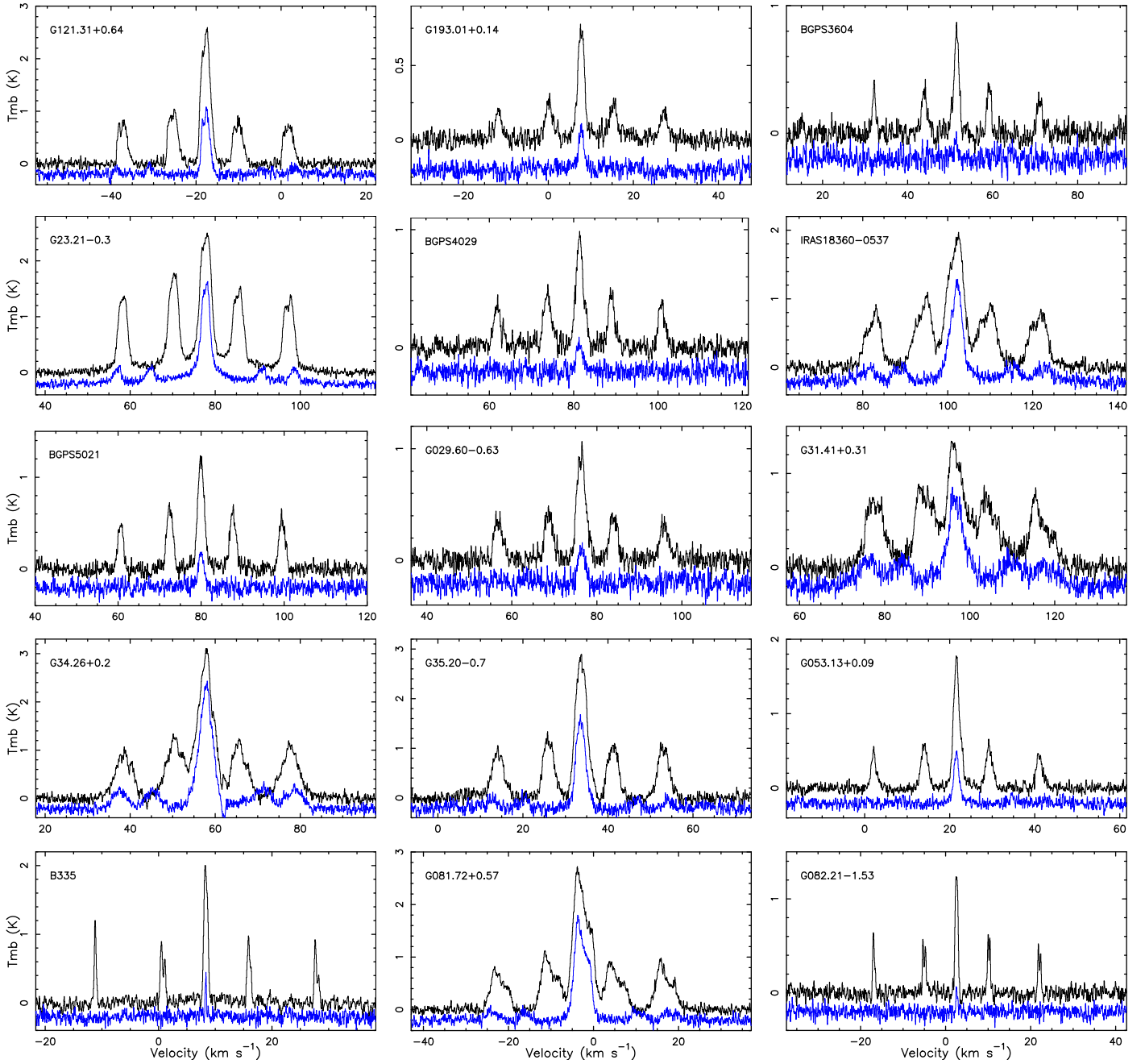
We conducted deep observations of the ammonia hyperfine intensity anomalies (HIAs) with the Effelsberg 100 m telescope in fifteen infall source candidates. By adopting a rational definition of the HIA proposed by Zhou et al. (2020), we seek to test whether HIAs can be used to trace infall motions, in particular of the cold molecular gas. Due to long integration times on the targets, all the  $\text{NH}_3$  satellite lines are clearly detected and all the HIAs of the inner ( $HIA_{IS}$ ) and outer ( $HIA_{OS}$ ) satellite lines are derived. In 14 out of 15 targets, either  $HIA_{IS}$  or  $HIA_{OS}$  values deviate from unity (indicating an anomaly) by more than their  $1-\sigma$  uncertainties. In 10 targets, both  $HIA_{IS}$  and  $HIA_{OS}$  values exceed their  $1-\sigma$  uncertainties. Thus the presence of HIAs is prevalent in our sample. Meanwhile, all the derived HIAs remain within the framework of the existing two models, the hyperfine selective trapping (HST) and systematic contraction or expansion motions (CE) models. It is found that a majority of the HIAs in the sources likely harboring infall motions are still consistent with the HST model. In three sources, HIAs are consistent with infall motions under the CE model, while a procedure mitigating effects of the HST model even uncovers six such sources. Therefore, HIAs could be used as an infall tracer but seem to be not highly sensitive to infall motions in our single-dish observations. Nevertheless, akin to the case of blue-skewed profiles, HIAs might be blended with emission from outflow activities, since ammonia emission is also commonly seen in outflows.

HIAs induced by the HST model are expected to be enhanced with increasing kinetic temperatures ( $T_K$ ).  $HIA_{IS}$  and  $HIA_{OS}$  in our observations may show higher anomalies with increasing  $T_K$ , but the correlations are weak. On the contrary, HIAs induced by infall motions seem to show relatively constant values against  $T_K$ , suggesting that HIAs might serve as more effective infall tracers for relatively cold gas. High-resolution observations of HIAs are crucial to further constrain the origin of HIAs and assess the contributions from infall and outflow motions.

*Acknowledgements.* We thank the anonymous referee for useful suggestions improving the paper. Based on observations with the 100-m telescope of the MPIfR (Max-Planck-Institut für Radioastronomie) at Effelsberg. This work was funded by the National Key R&D Program of China (No. 2022YFA1603103), the CAS “Light of West China” Program (No. 2021-XBQNXZ-028), the National Natural Science foundation of China (Nos. 12103082, 11603063, and 12173075), and the Natural Science Foundation of Xinjiang Uygur Autonomous Region (No. 2022D01A362). GW acknowledges the support from Youth Innovation Promotion Association CAS.

## References

- Beltrán, M. T., Rivilla, V. M., Cesaroni, R., et al. 2022, *A&A*, 659, A81  
 Camarata, M. A., Jackson, J. M., & Chambers, E. 2015, *ApJ*, 806, 74  
 Calahan, J. K., Shirley, Y. L., Svoboda, B. E., et al. 2018, *ApJ*, 862, 63  
 Cabedo, V., Maury, A., Girart, J. M., et al. 2021, *A&A*, 653, A166  
 Di Francesco, J., Myers, P. C., Wilner, D. J., et al. 2001, *ApJ*, 562, 770  
 Evans, N. J. 1999, *ARA&A*, 37, 311  
 Evans, N. 2003, *SFChem 2002: Chemistry as a Diagnostic of Star Formation*, 157  
 Evans, N. J., Di Francesco, J., Lee, J.-E., et al. 2015, *ApJ*, 814, 22  
 Ginsburg, A. & Mirocha, J. 2011, *Astrophysics Source Code Library*. ascl:1109.001  
 Henkel, C., Jethava, N., Kraus, A., et al. 2005, *A&A*, 440, 893  
 Ho, P. T. P., & Townes, C. H. 1983, *ARA&A*, 21, 239  
 Immer, K., Li, J., Quiroga-Núñez, L. H., et al. 2019, *A&A*, 632, A123  
 König, C., Urquhart, J. S., Csengeri, T., et al. 2017, *A&A*, 599, A139  
 Leung, C. M. & Brown, R. L. 1977, *ApJ*, 214, L73. doi:10.1086/182446  
 Longmore, S. N., Burton, M. G., Barnes, P. J., et al. 2007, *MNRAS*, 379, 535  
 Lu, X., Zhang, Q., Liu, H. B., Wang, J., & Gu, Q. 2014, *ApJ*, 790, 84  
 Mac Low, M.-M. & Klessen, R. S. 2004, *Reviews of Modern Physics*, 76, 125  
 Matsakis, D. N., Brandshaft, D., Chui, M. F., et al. 1977, *ApJ*, 214, L67  
 Ott, M., Witzel, A., Quirrenbach, A., et al. 1994, *A&A*, 284, 331  
 Park, Y.-S. 2001, *A&A*, 376, 348  
 Peretto, N. & Fuller, G. A. 2009, *A&A*, 505, 405  
 Qiu, K., Zhang, Q., Beuther, H., et al. 2012, *ApJ*, 756, 170  
 Rydbeck, O. E. H., Sume, A., Hjalmarsen, A., et al. 1977, *ApJ*, 215, L35  
 Shu, F. H. 1977, *ApJ*, 214, 214  
 Stutzki, J. & Winnewisser, G. 1985, *A&A*, 144, 13  
 Svoboda, B. E., Shirley, Y. L., Battersby, C., et al. 2016, *ApJ*, 822, 59  
 Tafalla, M., Myers, P. C., Caselli, P., et al. 2004, *A&A*, 416, 191  
 Watson, D. M. 2020, *Research Notes of the American Astronomical Society*, 4, 88  
 Wielen, M., Wyrowski, F., Menten, K. M., et al. 2018, *A&A*, 609, A125  
 Winkel, B., Kraus, A., & Bach, U. 2012, *A&A*, 540, A140  
 Wu, G., Qiu, K., Esimbek, J., et al. 2018, *A&A*, 616, A111  
 Wu, G., Henkel, C., Xu, Y., et al. 2023, *A&A*, 677, A80  
 Wyrowski, F., Güsten, R., Menten, K. M., et al. 2012, *A&A*, 542, L15  
 Wyrowski, F., Güsten, R., Menten, K. M., et al. 2016, *A&A*, 585, A149  
 Xu, Y., Bian, S. B., Reid, M. J., et al. 2021, *ApJS*, 253, 1  
 Yang, Y., Jiang, Z.-B., Chen, Z.-W., et al. 2020, *Research in Astronomy and Astrophysics*, 20, 115  
 Yang, Y., Jiang, Z., Chen, Z., et al. 2021, *ApJ*, 922, 144  
 Yang, W. J., Menten, K. M., Yang, A. Y., et al. 2022, *A&A*, 658, A192  
 Yoo, H., Kim, K.-T., Cho, J., et al. 2018, *ApJS*, 235, 31  
 Zhang, Q., Hunter, T. R., & Sridharan, T. K. 1998, *ApJ*, 505, L151  
 Zhang, Q., Sridharan, T. K., Hunter, T. R., et al. 2007, *A&A*, 470, 269  
 Zhou, S., Evans, N. J., Koempe, C., et al. 1993, *ApJ*, 404, 232  
 Zhou, D., Wu, G., Esimbek, J., et al. 2020, *A&A*, 640, A114

Appendix A: Observed  $\text{NH}_3$  ( $J, K$ ) = (1, 1) and (2, 2) spectra.

**Fig. A.1.**  $\text{NH}_3$  ( $J, K$ ) = (1, 1) and (2, 2) spectra. The observed  $\text{NH}_3$  ( $J, K$ ) = (1, 1) and (2, 2) spectra are shown in black and blue colors in each panel.  $\text{NH}_3$  ( $J, K$ ) = (2, 2) spectra are shifted to -0.2 K on the Y-axis. The source name is labeled in the top-left corner of each panel.